Glass-Type Polyamorphism in Li-Garnet Thin Film Solid State Battery Conductors

Iñigo Garbayo, Michal Struzik, William J. Bowman, Reto Pfenninger, Evelyn Stilp, and Jennifer L. M. Rupp**

Ceramic $Li_7La_3Zr_2O_{12}$ garnet materials are promising candidates for the electrolytes in solid state batteries due to their high conductivity and structural stability. In this paper, the existence of "polyamorphism" leading to various glass-type phases for Li-garnet structure besides the known crystalline ceramic ones is demonstrated. A maximum in Li-conductivity exists depending on a frozen thermodynamic glass state, as exemplified for thin film processing, for which the local near range order and bonding unit arrangement differ. Through processing temperature change, the crystallization and evolution through various amorphous and biphasic amorphous/crystalline phase states can be followed for constant Li-total concentration up to fully crystalline nanostructures. These findings reveal that glass-type thin film Li-garnet conductors exist for which polyamorphism can be used to tune the Li-conductivity being potential new solid state electrolyte phases to avoid Li-dendrite formation (no grain boundaries) for future microbatteries and large-scale solid state batteries.

Dr. I. Garbayo,[+] Dr. M. Struzik, Dr. W. J. Bowman, R. Pfenninger, Dr. E. Stilp, Prof. J. L. M. Rupp
Electrochemical Materials
Department of Materials
ETH Zürich
Hönggerbergring 64, Zürich 8093, Switzerland
E-mail: igarbayo@irec.cat; jrupp@mit.edu

Prof. J. L. M. Rupp
Electrochemical Materials
Department of Electrical Engineering and Computer Science
Massachusetts Institute of Technology
77 Massachusetts Avenue, Cambridge, MA 02139, USA

Dr. M. Struzik, R. Pfenninger, Prof. J. L. M. Rupp
Department of Material Sciences and Engineering
Massachusetts Institute of Technology
77 Massachusetts Avenue, Cambridge, MA 02139, USA

Dr. W. J. Bowman
Laboratory for Electrochemical Interfaces
Department of Nuclear Science and Engineering
Massachusetts Institute of Technology
77 Massachusetts Ave., 13-3066, Cambridge, MA 02139, USA

Dr. E. Stilp
Materials for Energy Conversion
Empa.
Überlandstrasse 129, Dübendorf 8600, Switzerland

[+]Present address: Area of Advanced Materials for Energy Catalonia Institute for Energy Research (IREC), Jardins de les Dones de Negre 1, 2ª pl. 08930 Sant Adrià de Besòs, Barcelona, Spain

DOI: 10.1002/aenm.201702265

1. Introduction

The next generation of energy storage devices relies on a broad and flexible range of volumetric and gravimetric energy densities to overcome the challenges in stationary, mobile, and portable electricity supply.[1,2] Here, all-solid-state batteries based on ceramic Li-conducting electrolytes have great potential as they allow for complete liquid-free battery architectures. Moving to all-solid-state brings significant advantages, among which their increased thermal stability and high energy density stand out. It is widely recognized that solid state batteries provide a wide thermal operation window of more than 400 °C, superior to liquid/polymer-based electrolytes that are often restricted to 120 °C as a maximum during operation.[3–5] The improved thermochemical stability gives opportunity to employ alternative high-voltage electrode materials, which are often instable toward standard liquid-based Li-battery electrolytes but provide higher capacity (see review by Dudney group [6]). Moreover, it opens up the possibility for the use of industrial waste heat for stationary power supply, which could be used to improve charging times and Li^+ diffusion for high performances with zero effective energy consumption.[7,8] Altogether, higher performances could be reached on a solid state battery system with better packaging (no liquid components) and higher safety (no potential leakages).

1.1. Opportunities for Microbattery Designs: All Solid State Ceramic Thin Film Architectures

Employing solid state electrolytes also opens the avenue for new Li-conducting oxide materials transferrable to thin film structures in the sub-micrometer regime for new microbattery architectures.[9–11] Microbatteries are particularly attractive as on-chip energy supply, for powering portable units where information is measured, exchanged, or stored at high volumetric densities. Nowadays, three main material designs are pursued for the fabrication of a microbattery: (i) liquid-based microbattery, (ii) hybrid polymer membrane microbattery, or (iii) all solid state microbattery thin film architectures. The difference between them remains mainly in their electrolyte's state of matter and packaging of the cell.

Liquid-based microbatteries are composed of microfabricated solid electrode structures deposited on a supporting substrate, and an ionic liquid electrolyte in contact with them. Here, recently published work by the Lewis group is to be highlighted.[12] For lab-on-a-chip integration, this approach still entails important design restrictions, since a relatively high volume is needed to host the liquid electrolyte and minimum feature size is still restricted to several µm. In hybrid polymer membrane microbatteries, a polymeric electrolyte membrane is included between the solid electrodes, swollen with liquid solvent, and a Li salt. From a miniaturization perspective, the main advantage is the possibility of stacking all the functional thin films on top of a supporting substrate. This opens new avenues for advanced microbattery designs ranging from planar, cross-plane to corrugated architectures with increased storage capacity.[13–15] Nevertheless, the presence of liquids in the system still derives some important restrictions, e.g., risk of leakages and temperature limitations.

Opposed to those, all solid state thin film microbatteries are completely based on solid state materials for all microbattery components, i.e., electrolyte and electrodes. This way, full transferability to thin film structures is possible, with less than 1 µm in total thickness (**Figure 1**a). This means a reduction of the electrode separation by more than 2 orders of magnitude compared to the other two microbattery approaches. It shortens significantly the Li diffusion pathways and increases the packaging density of the solid state microbattery units, all at the advantage of full silicon processing compatibility for complete integration into microelectromechanical system technologies.[16] By optimizing the microbattery design, the most important issues associated with all solid state microbattery operation can be overcome, namely, their internal resistance (lower Li conductivity of solid state electrolytes compared to liquid ones), mechanical stability, volume expansion, or strain adaptation during lithiation/delithiation processes. As an example, a recent review by Oudenhoven et al.[10] highlighted the possibilities of 3D architectures also for thin film solid state microbatteries. The integration of thin solid state electrode and electrolyte films in microfabricated Si-based architectures has lately been investigated by Notten's group.[10,17–19] Based on planar designs, several research groups have recently shown the successful fabrication of thin film microbatteries mainly using the lithium phosphorus oxynitride solid electrolyte originally developed at the Oak Ridge National Laboratory, see, e.g., NanoEnergy thin film battery (Front Edge Technology, Inc.), Excellatron Solid State LLC. thin film battery, or more recently ref. [20]. In conclusion, in view of this analysis we see potential of solid state thin film microbatteries for Si-integrated lab-on-a-chip battery prototypes. However, the careful selection of solid electrolyte materials and their integration to full solid state microbattery designs are still to be made giving perspective for fast Li diffusion and highest energy density for safe energy storage.

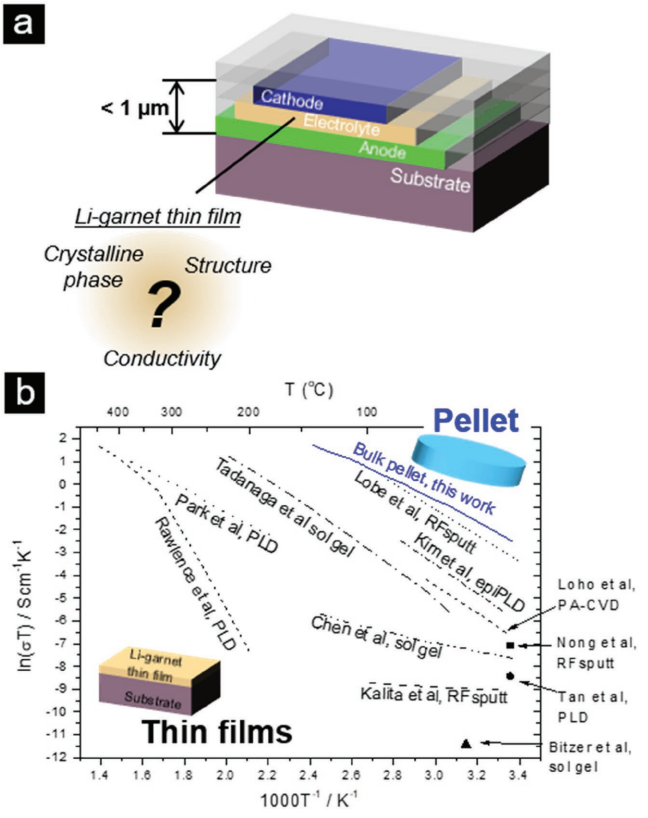

Figure 1. a) Schematic representation of a simple planar thin film-based microbattery. b) Arrhenius representation of reported $Li_7La_3Zr_2O_{12}$-based thin film in-plane conductivity,[45–56] compared to the bulk conductivity measured on a home-made cubic-garnet $Li_{6.19}Al_{0.28}$ $La_3Zr_{1.75}Ta_{0.25}O_{12}$ pellet.

1.2. Li-Garnet Solid State Electrolyte Materials: Perspectives for Microbattery Thin Films

Recent efforts on sintered ceramic pellet processing show novel fast Li^+ conducting materials employable as electrolytes in solid state batteries.[21,22] Among those solid state conductors, Li-stuffed cubic garnet ceramics,[23] and in particular those based on $Li_7La_3Zr_2O_{12}$ (LLZO) variants with cubic structure,[24] have been shown to be one of the most promising candidates for solid state batteries. High Li^+ conductivity of ≈1 mS cm^{-1} with structural stability upon cell loads has been reported,[23,25] positioning LLZO as one of the best Li^+ solid state conductors so far. Chemical stability against metallic Li,[24,26,27] oxide-based anodes[25] and high voltage cathodes[28,29] have been reported, showing the possibility of using the material in a very wide operational voltage window. Opposed to that, the penetration of Li dendrites onto the LLZO pellets has however been recently reported for some particular cases,[30] which might require surface modification of the electrode/electrolyte interface[31,32] or alternative approaches to vary the LLZO microstructures.

$Li_7La_3Zr_2O_{12}$ exhibits phase polymorphism with a more resistive tetragonal phase (σ_{Li+} ≈10^{-6} S cm^{-1}) stable at room temperature and a highly conductive (up to σ_{Li+} ≈10^{-3} S cm^{-1}) cubic phase above 750 °C. Highly conductive cubic phases can however be stabilized at low temperatures by adding dopants on either the Li, La, or Zr site,[23] obtaining either the cubic garnet Ia-3d space group directly or an acentric cubic I-43d space group (observed for Ga-stabilized LLZO; see ref. [33]). Probably the most promising and therefore most explored is the doping of the lithium structural sites of the garnet by either

Table 1. Literature review of $Li_7La_3Zr_2O_{12}$-based garnet thin films.

Reference	Year	Initial bulk garnet material	Deposition method	Substrate	Crystalline phase		Conductivity [S cm^{-1}]		
					As-deposited	Postannealed (temperature, [°C])	T = 25 °C	T = 300 °C	Activation energy [eV]
Kalita et al.[48]	2012	Undoped $Li_7La_3Zr_2O_{12}$	RF sputtering	SiO_2/Si + SUS electrode	Amorphous	–	4×10^{-7}	–	0.70
Nong et al.[49]	2015	Undoped $Li_7La_3Zr_2O_{12}$ + $Li_{0.33}La_{0.56}TiO_3$	RF co-sputtering	ITO/glass	Amorphous	–	2.83×10^{-6}	–	–
Katsui and Goto[51]	2015	Undoped $Li_7La_3Zr_2O_{12}$	MO-CVD	Al_2O_3	–	Cubic/tetragonal garnet 750–950 °C	–	–	–
Tan and Tiwari[54]	2012	Undoped $Li_7La_3Zr_2O_{12}$ +Li_2O	PLD (multilayers)	$SrTiO_3$, sapphire	Amorphous	Cubic garnet 1000 °C	7.36×10^{-7} (pulsed-laser annealed)	–	0.32
Park et al.[55]	2015	Undoped and Al-doped $Li_7La_3Zr_2O_{12}$	PLD	Si, SiO_2, MgO, anodized Al_2O_3, sapphire	Mainly amorphous Cubic garnet observed in the surface (≈5 nm)	–	1.61×10^{-6}	1.79×10^{-3}	0.35
Loho et al.[52]	2017	Undoped $Li_7La_3Zr_2O_{12}$	CO_2-laser-assisted CVD	Pt, Si	Tetragonal garnet	–	4.2×10^{-6}	–	0.50
Chen et al.[45]	2014	Al-doped $Li_7La_3Zr_2O_{12}$ solution	Sol–gel	Pt,Ti/SiO_2/Si	Amorphous	$La_2Zr_2O_7$ 600–800 °C	1.67×10^{-6} (annealed 600 °C)	–	0.18
Tadanaga et al.[46]	2015	Al-doped $Li_7La_3Zr_2O_{12}$ solution	Sol–gel	MgO	–	Cubic garnet 900 °C	2.4×10^{-6}	–	0.52
Kim et al.[53]	2013	Al-doped $Li_7La_3Zr_2O_{12}$	PLD	$Gd_3Ga_5O_{12}$	Cubic garnet, epitaxial	–	2.5×10^{-6} (001)-oriented 1.0×10^{-5} (111)-oriented	–	0.52
Rawlence et al.[56]	2016	Al-doped $Li_7La_3Zr_2O_{12}$	PLD	MgO	–	Cubic garnet to $La_2Zr_2O_7$, thickness dependent 600°C	–	8.3×10^{-4}	0.60
Lobe et al.[50]	2016	Ta-doped $Li_7La_3Zr_2O_{12}$	RF sputtering	Aluchrom YHf (electronic conductor)	Cubic garnet + impurities	–	2×10^{-9} (cross-plane) 1.2×10^{-4} (in-plane)	–	0.47
Bitzer et al.[47]	2016	Y-doped $Li_7La_3Zr_2O_{12}$	Sol–gel	Steel	Amorphous	Cubic garnet 800 °C in Ar	3.4×10^{-8} [45 °C]		–

Al[34,35] or Ga.[33,36–38] Regarding the zirconium structural site, Ta-doping has been shown as a good candidate for improving phase stability and Li^+ mobility by increasing the concentration of the vacancies on the Li sites.[39–44]

Despite the knowledge gained on LLZO pellet fabrication and synergy of lattice structure evolution and Li-transfer, the transferability of LLZO to thin film structures remains challenging. Only a few attempts to produce garnet-based thin films have been reported, which we review in **Table 1**: These are mainly LLZO garnet-type structures being undoped or doped with Al, Y, or Ta and deposited by either sol–gel,[45–47] sputtering,[48–50] metal-organic, or CO_2-laser-assisted chemical vapor deposition (MO-CVD, LA-CVD)[51,52] or pulsed laser deposition (PLD).[53–56] Figure 1b summarizes their Arrhenius-type conductivity characteristics. Here, in-plane conductivity of Li-garnet films is plotted and compared to the bulk conductivity of a home-made LLZO pellet co-doped with Al and Ta in the Li and Zr sites, respectively (being in good agreement with best conduction values in the literature[38]). Analyzing the literature on these Li-garnet thin films, we can conclude the following trends from Table 1 and Figure 1b.

First, there is a wide window of reported film Li conductivities for LLZO thin films, spanning over three orders of magnitude, from 10^{-7} to 10^{-4} S cm^{-1} at room temperature depending on the selected processing of the films. In fact, the majority of the reports reveal conductivities of 10^{-7}–10^{-6} S cm^{-1} for either undoped or Al-doped LLZO films and with different microstructures (amorphous, polycrystalline, epitaxial). Only a recent publication by Lobe et al.[50] reported a high in-plane conductivity of 1.2×10^{-4} S cm^{-1} at room temperature for sputtered Ta-doped LLZO films, i.e., being close to the bulk pellet conductivity. However, it is to be noted that in this case the measurement might be influenced by the usage of conducting substrate, and

it remains unclear whether the real in-plane conductivity of the LLZO film alone is measured. A wide range of activation energy of conductivity has also been reported, from 0.18 to 0.70 eV, and no clear dependencies of the activation energy such as with the doping level have been observed.

Second, all LLZO films show independently of the doping concentration a roughly one to three orders of magnitude lowered conductivity, when compared to bulk conductivities reported for the same material as large-scale ceramic pellets.[24] Similar observations of a lowered ionic conductivity for thin films, when compared to bulk pellets, are also known for other oxide systems, such as ceria or zirconia, which can be explained by the change in grain-to-grain boundary volume ratio alone, changes in strain state affecting ionic diffusion, and many other microstructural changes.[57–60]

Third, there are differences in the phase composition and crystallinity between the as-deposited LLZO films and postannealed ones. For example, Table 1 clearly highlights that almost all films published are amorphous when as-deposited. Till date, the general understanding coming from phase stability studies in Li-garnet pellets synthesized from pressed and sintered powders was that the cubic phase should be targeted to access a high ionic conductivity. Now, in the synthesis of a thin film LLZO structure a dense oxide structure is directly deposited, which differs substantially from the classic pellet processing where grain boundary and volume diffusion needs to be activated in the neck growth to form a dense ceramic body. Here, it remains unclear how the cubic garnet LLZO phases form in the dense and solid thin films, and whether postannealing treatments added after deposition are needed, since diffusion and phase formation kinetics can largely differ. Almost nothing is known on the near-order structures, growth, stability range, or Li-conduction of amorphous Li-garnet thin film structure even though these may be attractive due to their low-temperature processing for complementary metal–oxide–semiconductor (CMOS) integration. In addition, it can be concluded that after postannealing predominantly a mixture of lithiated LLZO garnet phases and delithiated $La_2Zr_2O_7$ (LZO) phases was obtained; see, e.g., Chen et al.[45] and Rawlence et al.[56] In fact, the appearance of the Li-deficient $La_2Zr_2O_7$ as secondary phase in annealed films is commonly observed for Li-garnet films,[45,46,51,55,56] but this is not yet clearly associated with any particular deposition process and the phase stability range simply needs to be explored for the films. Only Kim et al.[53] reported a direct epitaxial growth of cubic garnet Al-doped LLZO by PLD, and recently Lobe et al.[50] showed the growth of cubic Ta-doped LLZO garnet by radio frequency (RF) sputtering at 800 °C.

In addition, it is evident that the Li-concentration per film volume, which in turn affects the stability and probably also the crystallinity of the oxides, is not comparable based on the literature data analysis. This highlights the need for a more fundamental understanding on phase formation, crystallization and growth kinetics for LLZO-based thin films, their doping and processing. For example, there is indication from a recent systematic study on Al-doped LLZO films made by PLD that there is an optimum between the degree of Li concentration per film volume, stabilization of Li phase, dewetting, and connectivity of the grains in the microstructure; see Rawlance et al.[56] Also, Tadanaga et al., as well as recently Lobe *et al.* and Loho et al., quantified the Li content on the films by time of flight secondary ion mass spectroscopy (ToF-SIMS), showing the relevance of Li-loss compensation during annealing (for sol–gel films [46]) and deposition temperature (for sputtered films [50]) for phase formation.

Finally, one really important point in the analysis is that the as-deposited amorphous LLZO films, reported by Kalita et al.,[48] Nong et al.,[49] or Park et al.,[55] show conductivities comparable in their values around 10^{-7}–10^{-6} S cm^{-1} to those measured on films with cubic garnet phase by Kim et al.[53] (10^{-6} S cm^{-1}) or Tan and Tiwari[54] (10^{-7} S cm^{-1}). It remains unclear how Li-conductive networks form in dense thin films of LLZO, when crystallizing from amorphous glass-type structures to crystalline tetragonal or cubic garnet structures. We highlight that till date there is not much that we know about amorphous garnet phases as these were never explored in bulk pellet form but could on the other hand be perfectly suitable for Li-conducting thin film electrolytes at the advantage of low and CMOS compatible processing temperature.

In conclusion, analysis of LLZO thin films reported in the literature reveals the potential of Li-garnet as future electrolyte thin films for all solid state microbattery architectures. Still, the huge scattering reported in Li conductivity and activation energy is simply not yet suited for further engineering of a microbattery based on the published results. Understanding whether and how Li-conductivity proceeds in amorphous glass type to crystalline LLZO-garnet thin film microstructures is essential to assure processing guidelines in the making of future microbattery architectures. Fundamentally, this will also help to design and manipulate phase equilibriums, and advance amorphous glass-type to crystalline Li-garnet model structures; for example, Li-dendrites often hazardous to crystalline LLZO solid state batteries may be avoided by amorphous microstructures. In essence, deeper knowledge of the phase stability range, Li concentration, and Li^+ mobility from glassy to crystalline garnet thin films is needed to advance microbattery integration in the long run, strategies for low-temperature ceramic/glass processing, and also to learn about the role of grain boundaries for these LLZO electrolyte materials.

The aim of this work is to contribute to this knowledge by investigating the phase formation, nanostructure evolution, and Li-transport for aluminum and tantalum-doped Li-garnet films ($Li_{6.19}Al_{0.28}La_3Zr_{1.75}Ta_{0.25}O_{12-\delta}$ films, denoted in this paper as simply LLZO) grown by PLD. We explore the effect of PLD deposition conditions on the crystallization and ionic transport characteristics of the films, toward thin film phase stabilization and Li^+ mobility maximization. The amorphous versus crystalline properties of the LLZO and its implications on the Li^+ mobility are discussed in terms of long-range order versus near-range order crystal structures probed by X-ray diffraction (XRD), Raman spectroscopy, and detailed transmission electron microscopy (TEM) analysis. As highlighted before, a tremendous scatter over preparation and electrochemical properties is present for reported LLZO films; therefore, we intend to contribute through this work with model experiments studying the evolution and role of glassy to crystalline phases on Li conduction for Li-garnet films made by PLD. Ultimately, this work attempts to present amorphous garnet films as suitable candidates for thin film Li conducting electrolytes on all-solid state microbatteries.

2. Results and Discussion

2.1. Phase and Structure Evolution during Crystallization of Li-Garnet Thin Films

Thin films were deposited by PLD from a Li-garnet target of nominal stoichiometry $Li_{6.19}Al_{0.28}La_3Zr_{1.75}Ta_{0.25}O_{12}$ (LLZO) on top of a 500 nm thick Si_3N_4 dielectric layer on Si (**Figure 2**a). We exemplify the successful deposition of a dense and crack-free Li-garnet film microstructure deposited at 500 °C, in its cross-sectional scanning electron microscopy (SEM) image (Figure 2b). The Li-garnet microstructure reveals a dense film microstructure of 300 nm in thickness deposited on top of the Si_3N_4/Si substrate. There is a tendency to grow columnar grains, common for PLD depositions. Through the following, we probe the implication of deposition temperature variations from 50 to 750 °C on the phase and structural evolution of Li-garnet films for a fixed PLD background pressure of 0.013 mbar of O_2. Dense and crack-free film structures were similarly deposited in the whole temperature range up to 750 °C; see SEM details in Figures S1 and S2 of the Supporting Information.

We now turn to the structural investigation by XRD and Raman spectroscopy of the thin film series deposited at $T_d = 50$, 300, 500, and 750 °C (Figure 2c–e). For comparison, we also add the diffraction and Raman spectra characteristics for a LLZO ceramic pellet, which was used for the PLD deposition as its target, as well as reference values from the literature.[61,62] First, we analyze the structural long-range order and crystal structure evolution of the films via XRD. At low to intermediate deposition temperatures of 50 to 300 °C, only a wide halo can be observed at low incident angles, suggesting that the Li-garnet films deposited in that temperature lack long range order, and may be predominantly of amorphous nature. Once the deposition temperature increases to 500 °C for the LLZO film deposition, a low-intensity wide peak at $2\Theta = 28°$ appears. At the highest deposition temperature tested being 750 °C for the Li-garnet film, this peak develops much higher intensity and is accompanied by additional diffraction peaks appearing at $2\Theta = 47°$, 56°, and 59°. The set of peaks at 750 °C may be well correlated with the (222), (440), (622), and (444) diffraction lines of polycrystalline $La_2Zr_2O_7$ phase.[62–64] Note that peaks coming from the Si-based substrate and Au top electrodes (deposited for subsequent electrochemical characterization) are marked; see details in Supporting Information (Figure S3, Supporting Information). We conclude that in an initial deposition state at low temperatures below 500 °C crystallization is on-going

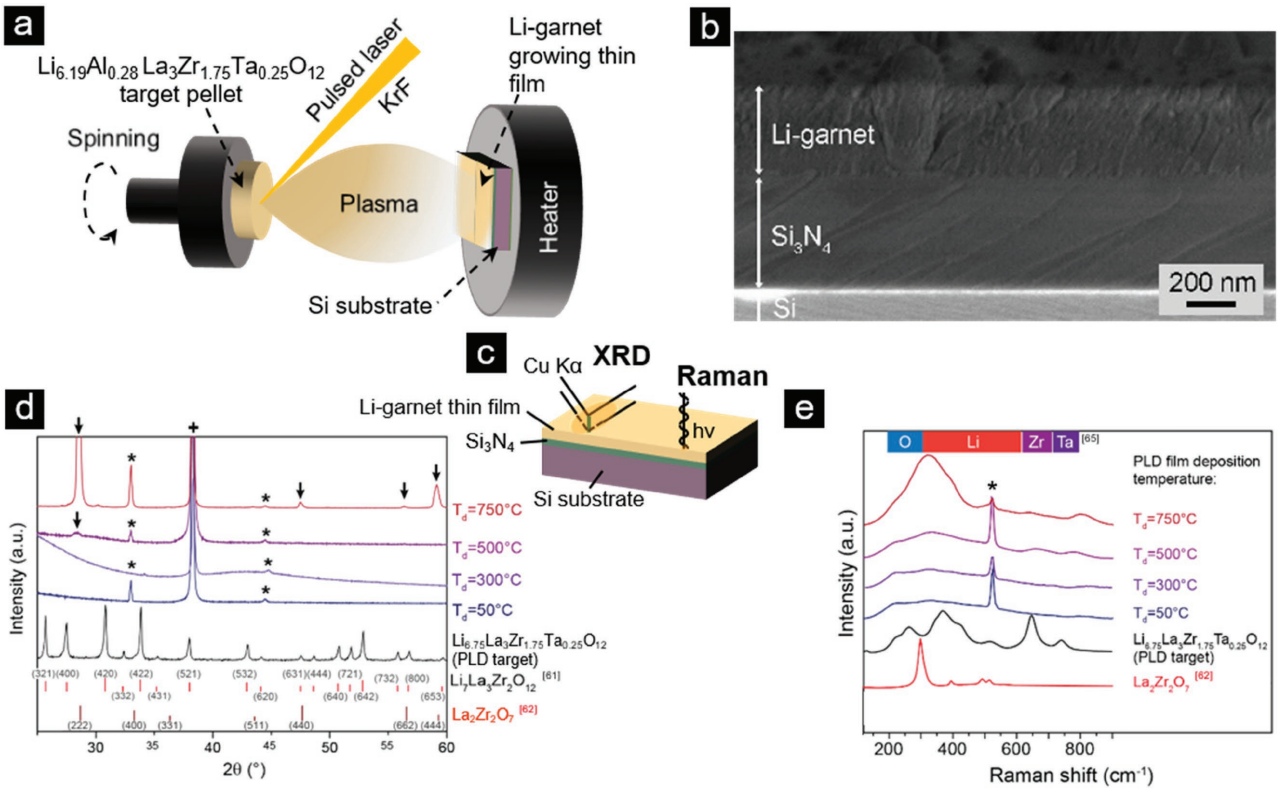

Figure 2. a) Schematic representation of a Pulsed Laser Deposition chamber where a Li-garnet film is being grown on top of a heated Si substrate. b) Cross-sectional view of a Li-garnet film deposited at $T_d = 500$ °C on Si_3N_4/Si substrate. c) Schematic view of the XRD and Raman measurement directions relative to the thin film, for long-order versus near-order structural analysis. d,e) X-ray diffractograms and Raman spectra of $Li_{6.19}Al_{0.28}La_3Zr_{1.75}Ta_{0.25}O_{12}$ target and thin films deposited by PLD on Si_3N_4/Si substrates at different substrate temperatures ($T_d = 50$, 300, 500, and 750 °C). Peaks assigned to the substrate (see Figure S3 in the Supporting Information) are indicated with "*". Peaks coming from Au electrodes deposited on top are denoted as "+"(only visible in XRD diffractograms). Reference diffraction planes and vibrational modes for cubic garnet $Li_7La_3Zr_2O_{12}$ and pyrochlore $La_2Zr_2O_7$ are also included for comparison.[61,62] Raman reference pattern of distorted fluorite $La_2Zr_2O_7$ is also added for better discussion. In (d), peaks appearing at the two highest temperatures are highlighted with arrows and lines.

in the Li-garnet structures, with the emergence of diffraction peaks indicative of either LLZO, $La_2Zr_2O_7$ phases, or mixtures thereof. Turning to higher deposition temperatures of 750 °C may lead to $La_2Zr_2O_7$ crystalline domains within the films.

Raman spectroscopy was then used to gain a better understanding of the amorphous to crystalline transition and the structural near-range order of the Li-garnet films. Figure 2e presents the Raman spectra of the thin films deposited at different temperatures. The Raman spectrum of the film deposited at T_d = 50 °C does not allow separation of vibrational modes coming from the thin film and those coming from the background. However, when increasing the deposition temperature to, respectively, T_d = 300 °C and T_d = 500 °C, the vibrational modes become more intense with the Raman modes' maximum peak positions at 212, 335, 670, and 783 cm^{-1}; see also Figure S4 (Supporting Information). This reflects the on-going crystallization and development of near-order structures measurable by Raman spectroscopy with increased deposition temperature. In general, we observe broadened peaks and strong Raman peak shifts if compared to the literature on micrograined and polycrystalline LLZO.[65] This can be explained by the fact that we have on the one hand amorphous or biphasic amorphous-crystalline phases in the thin film structures similar to a glass-ceramic and also small nanocrystallite sizes, for which strong shifts in the Raman bands are to be expected; see refs. [66] and [67] for details in other Raman-active systems. In accordance, the following Raman modes are suggested:

For low to intermediate temperatures T_d = 50–500 °C, we confirm the uprising of Raman active bands corresponding to the vibrational modes at 212 and 670 cm^{-1}. These modes may be ascribed to the T_{2g}/A_{1g} and A_{1g} bands characteristic for the oxygen bending (210 cm^{-1}) and Zr—O bond stretching (645 cm^{-1}) of the cubic LLZO, respectively;[65,68] see **Table 2**. Note that these are only active modes for the lithiated cubic-garnet-type LLZO structures, but would not be present for the $La_2Zr_2O_7$ phase, see ref. [62]. Consequently, the wide vibrational mode at 335 cm^{-1} could correspond to the T_{2g} band characteristic of the lithium-oxygen-related vibrations of the garnet, expected at 361 cm^{-1} for microcrystalline pellets.[68] In addition, we speculate that the vibrational mode at 783 cm^{-1} might be assigned to the A_{1g} band characteristic for the Ta—O bonds; see confirmation based on our reference Ta-doped cubic LLZO pellet showing a similar band at 750 cm^{-1} (and is in agreement with previous observations by Mukhopadhyay et al.[69]). Pronounced blueshifts and peak broadenings are observed for this bond as well as for the Zr—O bond stretching. These are likely to be attributed to the amorphous phase present, high film strain levels, and/or nanoscopic crystallites forming in a film matrix, as commonly observed in other complex oxide thin films.[70,71] Turning to the highest deposition temperature, T_d = 750 °C, the Raman peaks become more intense, in line with the higher crystallinity observed by XRD. In this state, the most intense peak is observed at 330 cm^{-1} and two additional peaks appear at 645 and 800 cm^{-1}. These two last peaks at high wavenumbers were also observed on the thin films deposited at lower temperatures and could be assigned to the Zr—O and Ta—O bond vibrations of the garnet. The wide intense peak at 330 cm^{-1} could also correspond to the bands characteristic of the lithium-oxygen vibration modes of the garnet (300–600 cm^{-1}). However, we note here that this peak might also be correlated with the F_{2g} vibrational mode of pyrochlore $La_2Zr_2O_7$, appearing at 299 cm^{-1} (Table 2). This would be in accordance with the observation of LZO crystallization at the highest deposition temperature by XRD, and it would match with the systematic blueshift observed for the rest of the peaks. Still, the presence of the additional peaks at 645 and 800 cm^{-1}, only attributable to the garnet, as well as the clear peak shoulders at 212 and 394 cm^{-1} suggests that the band at ≈330 cm^{-1} would be not only due to the $La_2Zr_2O_7$ but rather a combination of vibrations from both lithiated LLZO and LZO phases at a higher degree of crystallinity.

In conclusion, based on structural analysis of long and near order by XRD and Raman spectroscopy we conclude that for low-temperature depositions of ambient to T_d = 500 °C an amorphous lithiated garnet network exists with a measurable local cubic-structure-type $Li_7La_3Zr_2O_{12}$ ordering (e.g., Raman, signature of coupled T_{2g} and A_{1g} bands). At higher deposition temperature of T_d > 500 °C, $La_2Zr_2O_7$ starts to crystallize in long-range order domains. Still, some lithiated LLZO phase with certain near-range ordering appears to be present even in the films deposited at the highest temperature, T_d = 750 °C (e.g., presence in Raman spectrum of typical Ta—O and Zr—O vibrational modes of the garnet).

Table 2. Energy (cm^{-1}) and tentative symmetry assignments of Raman modes of Li-garnet thin films deposited at the two highest temperatures tested. (*) 735 cm^{-1} vibrational mode is ascribed to A_{1g} stretching of Ta—O bond based on home-made reference.

Symmetry (tentative)		Reference		Thin film deposition T	
LLZO	$La_2Zr_2O_7$	LLZO[65]	$La_2Zr_2O_7$[62]	750 °C [cm^{-1}]	500 °C [cm^{-1}]
				(this study)	
T_{2g}		209		212	212
A_{1g}		251			
	E_g		299	330	335
T_{2g}		361			
	F_{2g}		394	394	–
E_g/T_{2g}		410			
	A_{1g}		492	–	–
E_g/T_{2g}		514		–	–
	F_{2g}		516	–	–
A_{1g}		645		645	670
A_{1g}		735 (*)		800	783

2.2. Nanostructural and Li-Concentration Evolution of the Li-Garnet Thin Films during Crystallization

The phase and structure evolution of the Li-garnet thin films observed with respect to deposition temperature motivated us to carry out a detailed analysis of the nanostructures for the various amorphous to crystalline states by high resolution transmission electron microscopy (HRTEM) (**Figure 3**). We selected as model cases three Li-garnet films representing a low, medium, and high deposition temperature, viz. the films

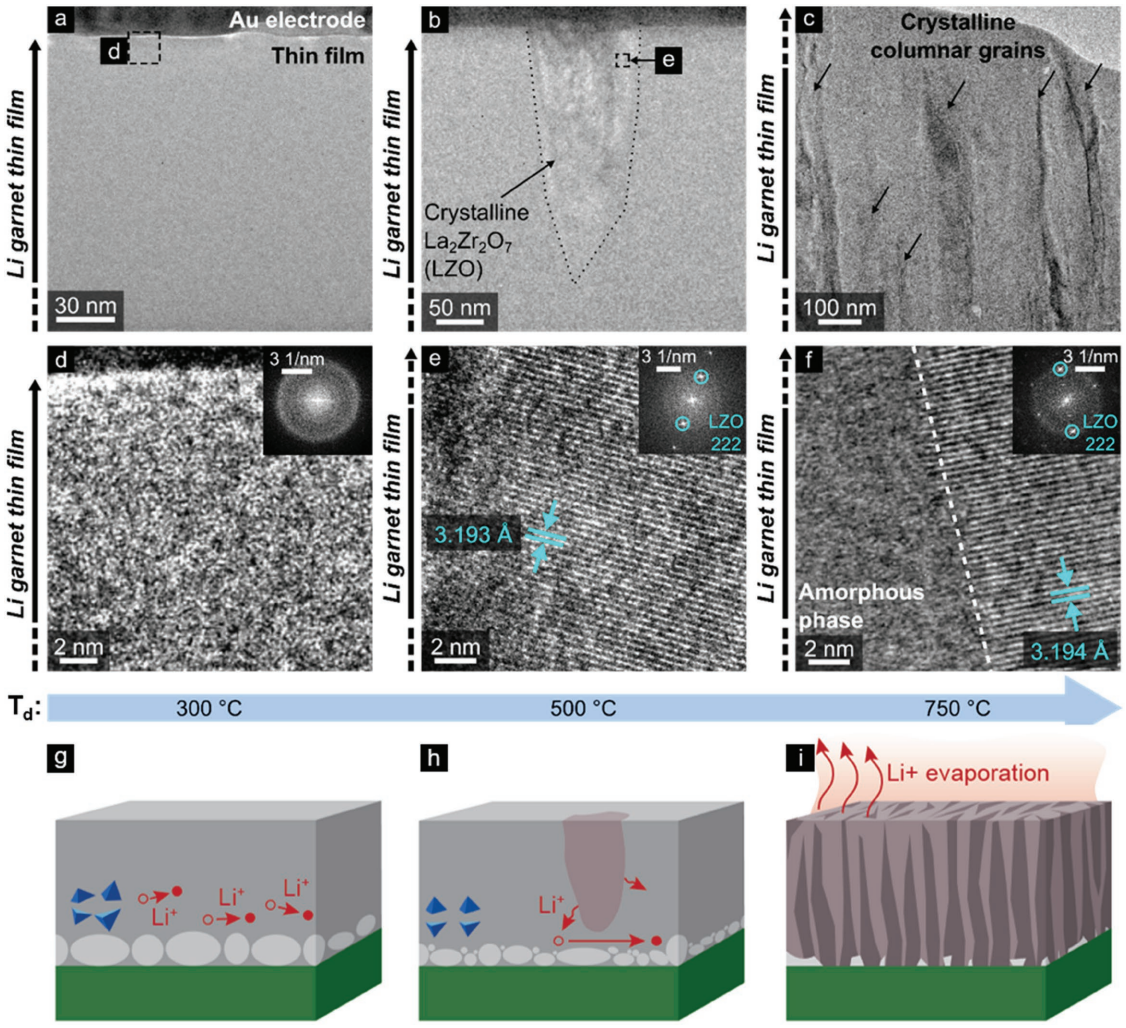

Figure 3. a–c) Low magnification and d–f) high resolution TEM images of thin films deposited at (a,d) 300 °C, (b,e) 500 °C , and (c,f) 750 °C. (a,d) Interface region between Au electrode and LLZO thin film, with inset diffractogram in (d). Image in (d) is acquired from the region highlighted in (a) with a dashed box. (b,e) Crystalline LZO inclusion (outlined with a dotted line) visible in noncrystalline matrix. Inset diffractogram in (e) shows highlighted diffraction spots indexed to the LZO (222) planes visible in the HRTEM image (e). Image (e) was acquired in region of (b) highlighted with a dashed box. c,f) Crystalline columnar grains (labeled with arrows) visible in noncrystalline matrix; phase boundary is highlighted in HRTEM image (f). Inset diffractogram in (f) is labeled to highlight the LZO (222) spots; see Figure S5 in the Supporting information for further analysis of this diffractogram. Schematics in g–i) represent the suggested film microstructures at T_d = 300, 500, and 750 °C.

deposited at T_d = 300, 500, and 750 °C. Figure 3 shows low (a–c) and high (d–f) magnification images of these three films, as well as selected area electron diffraction data from different regions of the films (insets in (d)–(f)).

At low deposition temperature, T_d = 300 °C, uniform mass-thickness contrast is visible in the thin film at low magnification (Figure 3a). At high magnification (Figure 3d), contrast associated with atomic-scale disorder, recognizable as a random distribution of bright and dark spots, is observed. The inset diffractogram, a Fourier transform of the image, was computed from the provided high resolution image, and exhibits a number of concentric diffuse rings of intensity. The absence of Bragg spots from this pattern indicates that the film is noncrystalline and likely of amorphous nature. Considering the local diffraction information in light of the earlier Raman-based findings, it is likely that domains with a lithiated near order of cubic-type LLZO phase are present here. However, note that this comment is based on the measurement of garnet vibrational modes in Raman (Figure 2e), as we can only conclude from HRTEM (Figure 3d) that the film deposited at 300 °C is likely amorphous (Figure 3g).

For intermediate deposition temperature, T_d = 500 °C, Li-garnet films exhibit uniform image contrast at low magnification (Figure 3b), indicating its amorphous state, but also include regions of crystallinity. These crystalline regions visible in TEM images exhibit clear diffraction contrast distinguishable from the uniform mass-thickness contrast of the amorphous part of the Li-garnet film, exemplified by the area in Figure 3b outlined with a dotted line. High resolution images of these crystalline inclusions confirmed the presence of lattice fringes (Figure 3e) from which interatomic spacing could be measured. Analysis of diffractograms computed from these lattice

fringe HRTEM images, such as that in the inset of Figure 3e, indicated 3.193 Å lattice fringe spacing, which we attribute to the 3.12 Å (222) plane spacing of LZO.[72–75] Although there is a discrepancy between the reference (222) LZO plane spacing (see Table S1 in the Supporting Information) and those measured via HRTEM, this assignment is consistent with our XRD analysis in Figure 2d, which shows the presence of a peak that may match the (222) peak (at ≈28.6°) in the film deposited at 500 °C. Because the size of crystalline inclusions is many tens of nanometers, one can expect to detect them via XRD. The alternative assignment of the crystalline inclusions to LLZO is not adopted in this case because the LLZO plane spacings (see Table S1 in the Supporting Information) most closely matching that measured via HRTEM are (420) and (400),[34,76] and these peaks are not detected in our XRD analysis of this sample. From this analysis, we conclude that the microstructure of the film deposited at 500 °C is thought to be a lithiated amorphous nanostructure with local garnet near order containing crystalline grains of $La_2Zr_2O_7$ grains (Figure 3h).

Studying low-magnification images of the thin film deposited at high temperature T_d = 750 °C, microstructural features threading vertically through the film are visible, and are highlighted in Figure 3c with arrows. These features exhibit relatively strong diffraction contrast (darker contrast originating from crystalline regions) and are dispersed in a matrix of uniform image contrast, somewhat similar to the microstructure observed in images of the film deposited at T_d = 500 °C in Figure 3b. In the thin film deposited at T_d = 750 °C, these features are interpreted as crystalline columnar grains existing in an amorphous film nanostructure (Figure 3i) and are attributed to columnar grain growth typical of PLD processing.[77] Still, a rather unusual broad separation of the columns by tens of nanometer through the amorphous matrix of the film is observed. Hence, a classic grain boundary separating grains by distances of 1–2 nm on average has not formed yet. Figure 3f shows an HRTEM image of the phase boundary between a region of amorphous (left-hand side of dashed line) and a crystalline region (right-hand side). Like the film deposited at 500 °C, lattice fringes with 3.194 Å spacing are visible in the crystalline phase, and attributed to LZO (222) planes. In this specimen, intersecting lattice fringes were visible in HRTEM images, making it possible to compare measured diffractograms to computed diffraction spot patterns, as shown in Figure S5 (Supporting Information). Based on this analysis, we conclude that the crystalline columnar grains highlighted in Figure 3c are of the LZO phase separated still in this state by amorphous regions. Interestingly, regions of different contrast were found for the three films, T_d = 300 °C, T_d = 500 °C, and T_d = 750 °C, in the interface between the Li-garnet film and the Si_3N_4/Si substrate; see Figure S6 (Supporting Information). Scanning TEM annular dark field imaging confirmed that a porous region is apparently formed at these interfaces, which was found to be more pronounced in the case of T_d = 750 °C. However, this was not affecting the adherence of the film, and no delamination or cracking was observed as confirmed by SEM; see Figure 2b and Figures S1 and S2 (Supporting Information).

We now turn to ToF-SIMS to estimate the change in Li concentration with respect to the thermodynamic and phase

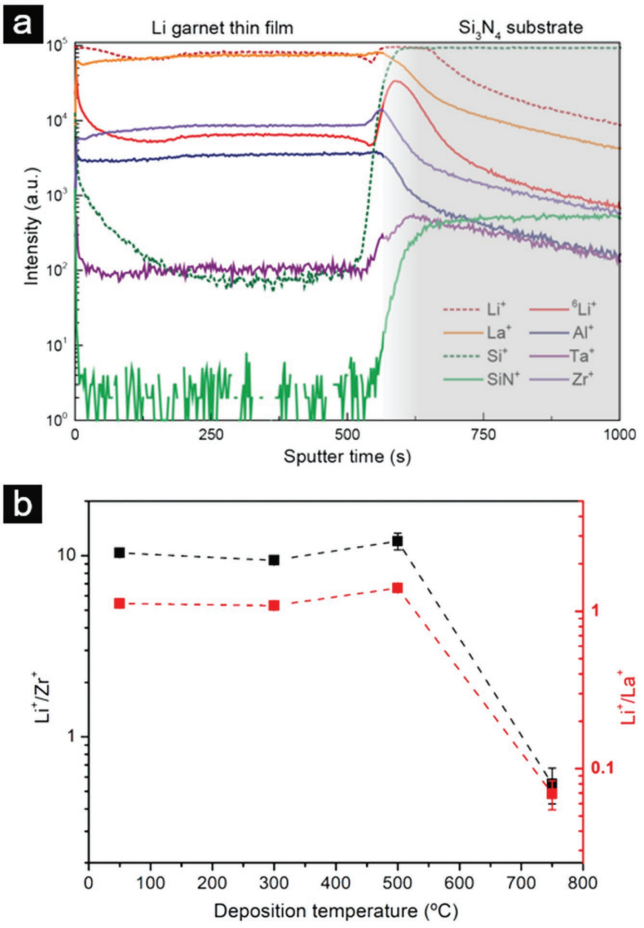

Figure 4. a) Time of flight secondary ion mass spectroscopy of a Li-garnet thin film deposited at T_d = 300 °C. All the relevant elements of the system, thin film and substrate, are plotted. b) Representation of the relative Li content as a function of the deposition temperature of the Li-garnet thin films. Both the Li^+ versus Zr^+ and the Li^+ versus La^+ are plotted for better comparison.

state, viz. the deposition temperature applied in processing of the Li-garnet films; see **Figure 4**. Here, we probe the depth-resolved qualitative composition along the whole thickness of the deposited films, until reaching the Si_3N_4/Si substrate. Figure 4a exemplifies the elemental analysis for an amorphous film deposited at T_d = 300 °C. By extracting the Li^+/Zr^+ and Li^+/La^+ ratios for the Li-garnet thin films (Figure 4b) we confirm that for low to intermediate deposition temperatures T_d = 50–500 °C both remain constant at 10.6 ± 1.3 and 1.19 ± 0.17, respectively. Interestingly, the appearance of LZO grains at T_d = 500 °C is not reflected in a lowering of Li to Zr/La ratio, thus suggesting the highest Li^+ concentration per volume unit on the amorphous part of those partially crystalline films. In contrast, for high temperature deposition at T_d = 750 °C, a sudden drop to 0.55 ± 0.12 and 0.069 ± 0.015 in the ratio of Li^+/Zr^+ and Li^+/La^+ is accessed. The ToF-SIMS results go in line with the Raman, XRD, and HRTEM findings, and highlight an interesting perspective, namely, that one can realize up to deposition temperatures of 500 °C various Li-garnet nanostructures of amorphous "glass-type" nature with a cubic-type

LLZO local order. Interestingly, one can manipulate their thermodynamic state to show within the amorphous matrix either no or first LZO grains forming, but keeping the total Li to Zr/La ratio constant. Only if first columnar grains form and proceed cross-sectionally through the film nanostructures, delithiation starts.

In conclusion, Li-garnet glass-type amorphous but dense film microstructures can be defined as either (i) purely Li-garnet cubic near order but grain-free films (low deposition temperature); (ii) mixed amorphous cubic-LLZO near-order structures with first forming grains of LZO close to the surfaces (intermediate deposition temperature); or (iii) crystalline dense films with columnar LZO grains and high interphase separation of tens of nanometer by amorphous Li-garnet phase (high deposition temperature). Now, to gain a more holistic understanding on the implication of these different microstructures on Li-diffusion, we turn to microcontacting and electrochemical impedance spectroscopy (EIS).

2.3. Conductivity for Glassy and Ceramic Li-Garnet Thin Films: The Implication of Polyamorphism and Crystallinity on Li Diffusion

In-plane electrochemical impedance spectroscopy was carried out on the thin film series by fabricating thin films on Si_3N_4/Si substrates with patterned top Au electrode films, as illustrated in **Figure 5**a. We analyze the influence of a purely amorphous but locally arranged Li-garnet structure, up to first loosely nonconnected grains and then blocking grain columns in the films, i.e., Li-garnet films deposited at T_d = 50, 300, 500, and 750 °C. The measurements were done on an in-plane geometry (Figure 5b). Figure 5c shows two exemplifying Nyquist plots acquired at measuring temperatures T = 310 and 380 °C, from a Li-garnet film deposited at T_d = 500 °C (see measurements for the whole film series in Figure S7 in the Supporting Information). One single artifact in the form of a depressed semicircle can be observed at high-to-medium frequencies (10^6–10^2 Hz). At low

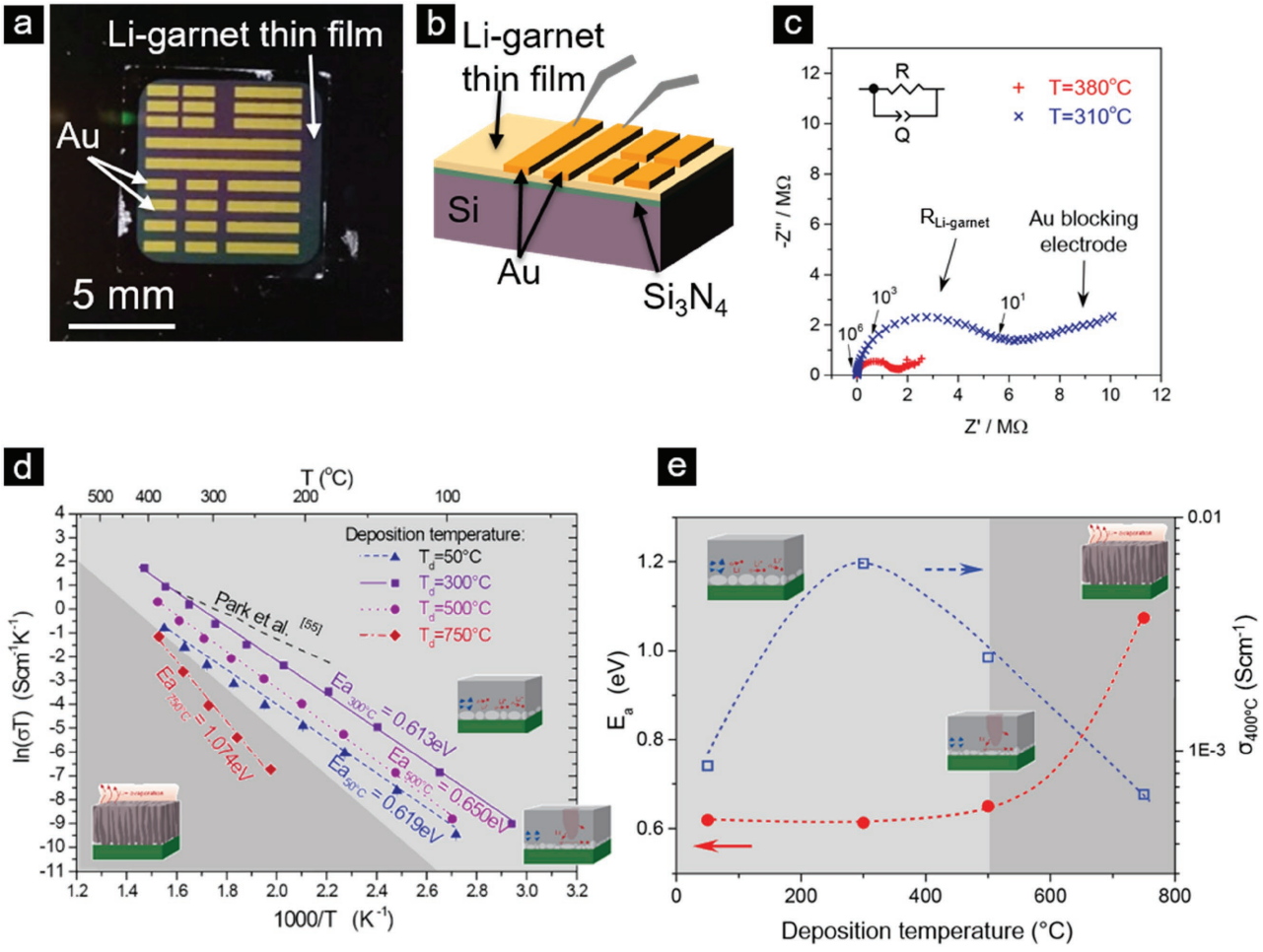

Figure 5. a) Top view optical image of a Li-garnet thin film deposited by PLD at T_d = 500 °C, with top Au electrodes (100 nm). b) Cross section schematic view of the sample analyzed with top in-plane electrode configuration. Grey tips represent the electrical contacts. c) Exemplary Nyquist plots acquired on one Li-garnet thin film deposited at T_d = 500 °C, measured at two different temperatures: T = 380 °C and T = 310 °C. Frequency decades (6, 3, 1) are indicated. d) Arrhenius representation of Li^+ conductivity measured on Li-garnet thin films deposited at different temperatures. e) Calculated activation energies (E_a) and conductivities at 400 °C ($\sigma_{400\,°C}$) as a function of the thin film deposition temperature. Two regions are identified and highlighted in different colors. Guidelines are included for better visualization.

frequencies this artifact is accompanied by a tale toward high impedance values. A resistor-constant phase element equivalent circuit model was used for fitting the high frequency artifact (see the inset of Figure 5c) and was assigned to the lithium ionic resistance associated with the thin film electrolyte. At the same time, the low frequency part of the Nyquist plot matches well with typical behavior of a blocking electrode and was therefore assigned to the top Au thin film electrodes. The total resistance of the electrolyte films obtained from the fitting of the high frequency semicircle was used for calculating the lithium conductivity as a function of temperature (Figure 5d). The figure shows in an Arrhenius representation the evolution of the Li^+ conductivities for the different thin films deposited at temperatures of T_d = 50, 300, 500, and 750 °C. Activation energies (E_a) and total conductivity dependences (at a measuring temperature of 400 °C) on the Li-garnet film deposition temperature are summarized in Figure 5e and collected in **Table 3**.

We purely analyze the effect of thin film deposition temperature and phase state on the total conductivity, ranging from various amorphous states to columnar crystalline (Figure 5d,e and Table 3). First, over all thin films we confirm a maximum in Li-conductivity and lower activation energy for films being in a specific amorphous "glass-type" state of the nanostructure with LLZO local near order according to Raman at a film deposition temperature of T_d = 300 °C. An activation energy of 0.613 eV and conductivity of 6.3(5) × 10^{-3} S cm^{-1} at T = 400 °C were measured on the films deposited at that temperature. Notably, we report for a constant Li concentration (according to ToF-SIMS), there exists an optimum at this deposition temperature where the "glassy-type" film structures develop a pure amorphous network showing features of near order along cubic local LLZO ordering (see Raman spectra; Figure 2e). Above or below, but still within the glassy-amorphous Li-garnet films, we confirm that the conduction drops as either the cubic near order LLZO network could locally not form enough (T_d = 50 °C), or first crystallites of LZO form as nonconnected grains in the film nanostructure (T_d = 500 °C). In other words, we report the existence of various states of "glass-type" Li-garnet networks in dense garnet thin films, for which the local near-order bonds and readiness to form local crystallites of LZO at the film interfaces define the overall lithium conductivity.

Second, turning to the analysis of the activation energies, as shown in Figure 5e, E_a evolves on the amorphous films from 0.619 eV on the films deposited at T_d = 50 °C to a minimum of 0.613 eV for T_d = 300 °C and then rising up again to 0.650 eV for the films deposited at T_d = 500 °C. Comparison of all these thin film "glass-type" model structures to literature of macrocrystalline bulk pellets reveals that measured activation energies, of around 0.6 eV, are comparable to those reported for bulk and total conductivities in LLZO-based pellets (0.3–0.7 eV; see Thangadurai et al.[23]). This would confirm that the conduction in low-to-intermediate deposition temperature amorphous garnet films is mainly Li^+ cationic. Still, the activation energy measured in this work for amorphous Li-garnet films is slightly higher than the one reported by Park et al.[55] also for PLD-deposited Li-garnet films. This difference might be related to the different initial garnet composition (Park et al. report on undoped and Al-doped Li-garnet films, but not Ta-doped). However, it is important to highlight that conduction at 400 °C is comparable for Park´s best performing film and the best Li-"glass-type" one reported here.

Finally, we observe a drastic increase of the activation energy to more than 1 eV when turning to the columnar and crystalline film deposited at T_d = 750 °C, while the total conductivity also significantly decreases. Here, we interpret that once grain columns penetrate across the film microstructure, the LZO phase dominates over the lithium diffusion pathway through the lithiated amorphous phase. In this sense, it is important to note that the higher activation energy measured at T_d = 750 °C; E_a ≈1 eV, is closer to reported values for O^{2-} conductivity in $La_2Zr_2O_7$.[78,79] This suggests that at high deposition temperatures ion migration turns from Li^+ cationic mobility in the garnet amorphous network to O^{2-} anionic mobility through the crystalline $La_2Zr_2O_7$. All in all, the amorphous structure types reported here show superior Li-conductivity and reveal that various states of amorphous phases exist for the garnets.

Table 3. Summary of most relevant properties of $Li_7La_3Zr_2O_{12}$-based garnet thin films prepared in this work.

Deposition temperature	Initial bulk garnet material	Deposition method	Substrate	Crystalline phase (as-deposited)	Conductivity [S cm^{-1}]			
					T = 25 °C (extrapolated)	T = 300 °C	T = 400 °C	Activation energy [eV]
50 °C	Ta,Al-doped $Li_7La_3Zr_2O_{12}$	PLD	Si_3N_4/Si	Amorphous garnet	2.86×10^{-9}	1.57×10^{-4}	7.51×10^{-4}	0.619
300 °C	Ta,Al-doped $Li_7La_3Zr_2O_{12}$	PLD	Si_3N_4/Si	Amorphous garnet	2.39×10^{-8}	1.18×10^{-3}	6.35×10^{-3}	0.613
500 °C	Ta,Al-doped $Li_7La_3Zr_2O_{12}$	PLD	Si_3N_4/Si	Amorphous garnet with crystalline $La_2Zr_2O_7$ inclusions	4.27×10^{-9}	4.19×10^{-4}	2.75×10^{-3}	0.650
750 °C	Ta,Al-doped $Li_7La_3Zr_2O_{12}$	PLD	Si_3N_4/Si	$La_2Zr_2O_7$ crystalline with amorphous garnet regions	1.11×10^{-13}	3.02×10^{-5}	2.07×10^{-4}	1.074

2.4. Model on Conduction, Phase, and Li Transfer for Li-Garnet Thin Films: From Polyamorphism to Crystalline Structures

In line with the structural and electrochemical analysis, a microstructural model is proposed for the PLD-deposited Li-garnet films as a function of the deposition temperature (**Figure 6**). At low-to-intermediate temperatures (T_d < 500 °C), an amorphous lithiated garnet nanostructure with certain near-order domains predominates on the films. Interestingly, the films deposited at 50, 300, and 500 °C differ, however, in their amorphous near-order structure, nanostructure, and electrochemical properties, while keeping constant Li content showing so-called "polyamorphism." We speculate here that a random network of local bonding units (LBUs) exists in all our films, similar to a polymer and also found in other complex oxides such as $BaTiO_3$ and $SrTiO_3$ perovskites; see the work of

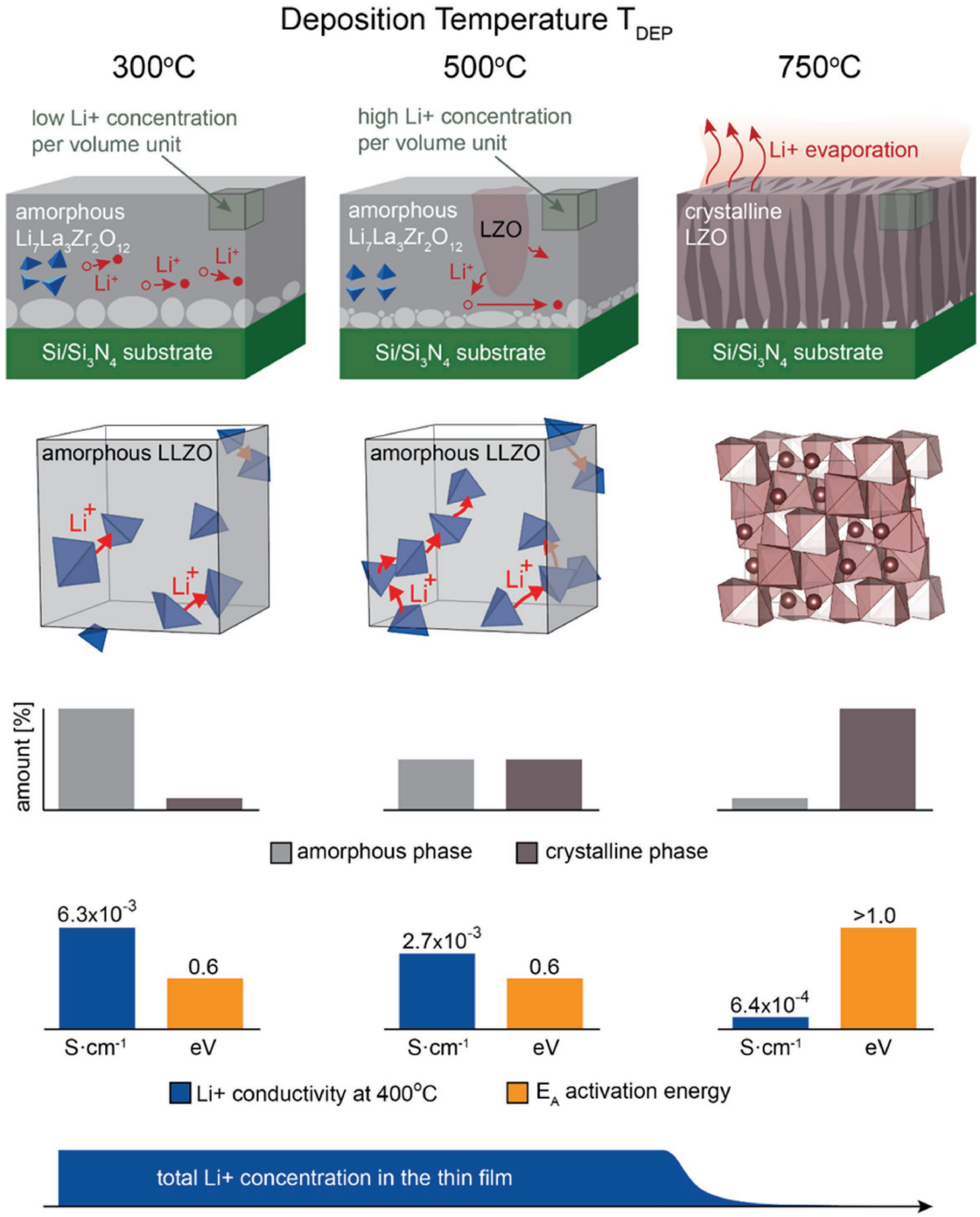

Figure 6. Schematic representation of the evolution with deposition temperature of thin film microstructure, crystallinity, conductivity, and Li content on Li-garnet thin films deposited by PLD.

Ehre and co-workers and Lubomirsky and co-workers.[80–82] Yet, different local alignment of Li tetrahedra and octahedra LBUs and their connection points lead to different Li-conduction properties depending on the deposition temperature for the garnets; this also differs to earlier reports on polyamorphic perovskites where entropy is lowered as only octahedra are varied in their connection. For the garnets, we report the existence of polyamorphism for which besides octahedra also tetrahedra contribute to the Li-conduction mechanism. Thus, at the lowest deposition temperatures of T_d = 50 °C the structure shows a higher disorder, the alignment of tetrahedra, and octahedra is poor and hence Li^+ conduction is low. Similar disordering at low deposition temperatures has also been described in the past for sputtered and evaporated ceramic oxide films.[83] When increasing the deposition temperature to T_d = 300 °C, higher Li^+ conduction is reached as a local rearrangement of the garnet LBUs occurs and tetra/octahedra alignment is optimum. A random network with certain near-range order where the Li^+ ions are located would facilitate the Li^+ hopping by a continuous re-adaptation of the local structure when the Li^+ is moving.[80] At higher deposition temperatures, T_d = 500 °C, single isolated crystalline $La_2Zr_2O_7$ grains start to crystallize embedded in the Li-garnet amorphous structure. The total Li content per volume is however still constant according to ToF-SIMS, which suggests a higher Li^+ concentration per volume unit in the amorphous part of the film. Paradoxically, this does not benefit for a higher Li^+ conductivity at this deposition temperature. On the contrary, the Li conductivity is slightly lower than that measured in the films deposited at T_d = 300 °C and the activation energy increases. This may be due to the presence of $La_2Zr_2O_7$ blocks that might increase the tortuosity for the Li^+ hopping and compensate the effect of the higher Li^+ concentration on the amorphous Li-conducting region. A new rearrangement of the position/rotation of the Li tetra/octahedra is also possible, which could be an added reason for the lowering of conductivity.

Finally, at T_d = 750 °C a clear crystalline columnar network of $La_2Zr_2O_7$ grains develops. Still, presence of amorphous regions between the crystalline grains is largely observed. However, at this point the amount of $La_2Zr_2O_7$ crystalline grains is large enough as to dominate the ionic conduction over the amorphous garnet network. As a consequence, the ionic mobility on those films turns from Li^+ cationic through the amorphous garnet structures (observed at T_d < 500 °C) to O^{2-} anionic mobility through the $La_2Zr_2O_7$ grains.

3. Conclusions

In this work, we demonstrate that "polyamorphism" exists besides crystalline states for thin film Li-garnet solid state battery electrolytes, and therein extend current knowledge that besides ceramic also glass-type Li-garnet phases exist. Looking forward, this offers exciting new opportunities to design for example grain boundary free amorphous and glass-type solid state battery electrolytes to avoid the often critical Li-dendrite formation leading to short circuiting of the cells. The thin film nature in processing of the glass and ceramic structure types successfully shown for the Li-garnets allows strong reduction in the internal resistance of the cell, and enables potential alternatives to classic liquid-type electrolytes.

Through the detailed study of the microstructural evolution of various amorphous to crystalline Li-garnet film on the example of PLD-deposited structures, the implication on Li^+ conductivity has been presented. We report the existence of polyamorphism for Li-garnets for which most likely the LBUs of octahedra and tetrahedra vary in their linking, affecting the Li-hopping and degree of entropy. In these thermodynamic "glassy" states, which can be accessed through changes in processing temperature, the overall Li-concentration remains constant (ToF-SIMS results) and it is purely the local near-order arrangement of the LBUs that affect the transfer of the ionic carriers (Raman spectroscopy results). Earlier studies on glass to ceramic evolution have reported the existence of polyamorphism for perovskite structures such as $BaTiO_3$ and $SrTiO_3$ perovskites—see Ehre and co-workers and Lubomirsky and co-workers—[80–82] for which various arrangements of octahedra LBUs have been confirmed by extended X-ray absorption fine structure (EXAFS). Here, we report for the first time that first garnet-type structures can also show polyamorphism for which the entropic degree is higher as tetrahedra and octahedra have to be arranged, and that a maximum in conductivity exists for a specific amorphous "glassy" state at intermediate processing temperatures that differs to structures processed above or below: in other words, "there are various shades of amorphous" for Li-garnets. Second, we extend today's considered Li-glass-type conductors such as LICGC from Ohara (Ohara Inc., Kanagawa, Japan), sulfide glasses,[84] or $A_{2.99}Ba_{0.005}O_{1+x}Cl_{1-2x}$ (A = Li, Na)[85] by the existence of glassy "polyamorphic" Li-garnet structure types.

Now it is obvious that the overall Li-conductivity of the Li-garnet films reported is in average below the one for macrocrystalline pellets, which we ascribe to the challenge to keep the overlithiation level for thin film processing. Notably, the reduced dimensions of the electrolyte on a thin film cross-plane configuration compared to the pellets (a reduction of more than four orders of magnitude is feasible) make these films already promising candidates for direct application in thin film microbatteries.

We see perspective that glass-type garnet electrolyte films are useful new Li-conductors to avoid Li-dendrite formation to improve safety and allow for full solid state battery architectures as microbatteries or large-scale battery systems.

4. Experimental Section

Thin Film Deposition: Li-garnet thin films were deposited by PLD (Surface Technologies) at different substrate temperatures, T_d = 50, 300, 500, and 750 °C, and a fixed background O_2 pressure of 0.013 mbar. A KrF excimer laser (TuiLaser, Germany) with wavelength 248 nm was used for the film deposition. Laser energy was set at 0.6 J cm^{-2} and the laser frequency at 10 Hz. The Li-garnet thin films were deposited on top of Si_3N_4/Si substrates. The Si_3N_4 dielectric layer was deposited by plasma enhanced CVD and had a final thickness of 500 nm.

A home-made pellet of nominal stoichiometry $Li_{6.19}Al_{0.28}La_3Zr_{1.75}Ta_{0.25}O_{12}$ was used as target. First, the Li-garnet powder was synthesized by solid state synthesis from LiOH, $La(OH)_3$, ZrO_2, Al_2O_3, and Ta_2O_5 precursors at 850 °C for 8 h. A pellet was then preformed in a cylindrical shape uniaxially and isostatically pressed at

22 000 bar for 10 min. Finally, the pellet was sintered at 1200 °C for 8 h in controlled O_2 atmosphere. The relative density of the sintered pellets was ≈94%.

Characterization of Crystal Structure: Crystal structure on the pellet was analyzed by means of X-ray diffraction (Bruker D8) in a typical Bragg-Brentano (θ–2θ) geometry, whereas for the thin films a grazing incidence geometry was utilized. The near-order structure of both thin films and pellets was analyzed by Raman spectroscopy (WiTec alpha 300 M+). All the data presented in this paper were acquired by using a 457 nm wavelength laser, applying 10 mW, and with a grating of 300 g mm^{-1}. Thin films deposited in Si_3N_4/Si substrates were measured on a cross-sectional configuration to minimize the strong Raman signal of the Si-based substrate. Baseline correction was applied to the final spectra, for better comparison and peak identification.

Microstructural Analysis: Top view and cross-sectional images of the thin films were taken by SEM (LEO 1530). Bright field TEM phase contrast imaging was performed using a Tecnai F30 operating with an accelerating voltage of 300 kV. TEM specimens were cross-sectional lamellas prepared by focused ion beam lift-out (FIB-SEM, Zeiss NVision 40). An Au electrode or protection layer was applied for FIB specimen preparation, and is visible in some of the micrographs (Figure 3a,b,d).

Compositional Analysis: For the depth-resolved qualitative compositional analysis ToF-SIMS was utilized, using a TOF.SIMS instrument from ION-TOF GmbH. During the ToF-SIMS analysis a selected sample region was bombarded with 25 keV Bi^+ primary ions in high vacuum, creating neutral, positively, and negatively charged particles. The charged particles were detected by a time-of-flight spectrometer to determine the composition of the sample surface to a depth of 1–2 nm. The profiling of the elemental composition in the depth was realized by layer-by-layer erosion with a second high current primary ion beam. In our measurement a 2 keV O_2^+ primary ion beam sputtered a grater of 500 μm × 500 μm. In order to avoid edge effects the analysis area was set to 200 μm × 200 μm in the center of the grater. An electron flood gun was used for charge compensation. The profiling is a switching between 2.6 s of sputtering and 100 μs of analyzing, which corresponds to a mass range of 1–820 u, with a waiting time of 0.5 s in between. The time-of-flight spectra were collected from positively charged particles by rasterizing the analysis area in a random pattern in 128 pixel × 128 pixel resolution with one shot per pixel. The emission current was stabilized to 1 μA.

Electrochemical Characterization: The electrochemical performance (Li^+ conductivity) of the Li-garnet thin films was studied by EIS (Zahner IM6). For that, gold electrodes of different lengths (1.5–7.5 mm) and distances (0.25–0.5 mm) between each other were e-beam evaporated (Evaporation Plassys II) on top of the Li-garnet thin films using a hard shadow mask. Au electrodes were then contacted with Au-coated tungsten tips on a temperature-controlled stage (Linkam HFS-600E) and an impedance spectrum was acquired every 50 °C from 100 to 450 °C with 10 min stabilization time for two consecutive heating and cooling cycles. Impedance was measured by applying an AC voltage of 50 mV and scanning in frequencies between 1 MHz and 0.1 Hz.

Supporting Information

Supporting Information is available from the Wiley Online Library or from the author.

Acknowledgements

The authors thank C. Thompson, MIT, for valuable discussion on nucleation and growth of Li-garnet oxide films. Special thanks go to I. Lubomirsky and D. Ehre and colleagues at the Weizmann Institute of Science for a great colloquium and discussion of local bonding units in polyamorphic oxide structures; J.L.M.R. comments that one can only recommend visits to Weizmann to seriously discuss the unusual and odd of experimental findings.

The authors thank the company ALSTOM for financial support and the Competence Center Energy and Mobility (CCEM) and Swisselectrics for funding the project: Proposal 911 "All Solid State Li-Ion Batteries Based on New Ceramic Li-Ion Electrolytes." W.J.B. was a Swiss Government Excellence Scholarship holder for the academic year 2015–2016 (ESKAS No. 2015.1183); and W.J.B. would like to acknowledge financial support of the US National Science Foundation's Graduate Research Fellowship Program (Grant No. DGE-1311230), as well as the US National Science Foundation's Graduate Research Opportunities Worldwide grant. The authors acknowledge support of ScopeM/Swiss Federal Institute of Technology ETHZ.

Conflict of Interest

The authors declare no conflict of interest.

Keywords

amorphous, electrolytes, garnets, polyamorphism, solid state batteries, thin films

Received: August 17, 2017
Revised: November 13, 2017
Published online: January 22, 2018

[1] J. M. Tarascon, M. Armand, *Nature* **2001**, *414*, 359.
[2] G. Pistoia, *Batteries for Portable Devices*, Elsevier Science, London **2005**.
[3] R. Bouchet, S. Maria, R. Meziane, A. Aboulaich, L. Lienafa, J.-P. Bonnet, T. N. T. Phan, D. Bertin, D. Gigmes, D. Devaux, R. Denoyel, M. Armand, *Nat. Mater.* **2013**, *12*, 452.
[4] Q. Hu, S. Osswald, R. Daniel, Y. Zhu, S. Wesel, L. Ortiz, D. R. Sadoway, *J. Power Sources* **2011**, *196*, 5604.
[5] X. Lin, R. Kavian, Y. Lu, Q. Hu, Y. Shao-Horn, M. W. Grinstaff, *Chem. Sci.* **2015**, *6*, 6601.
[6] J. Li, C. Ma, M. Chi, C. Liang, N. J. Dudney, *Adv. Energy Mater.* **2015**, *5*, 1401408.
[7] S. W. Lee, Y. Yang, H.-W. Lee, H. Ghasemi, D. Kraemer, G. Chen, Y. Cui, *Nat. Commun.* **2014**, *5*, 3942.
[8] F. Zhang, J. Liu, W. Yang, B. E. Logan, *Energy Environ. Sci.* **2015**, *8*, 343.
[9] J. B. Bates, N. J. Dudney, D. C. Lubben, G. R. Gruzalski, B. S. Kwak, X. Yu, R. A. Zuhr, *J. Power Sources* **1995**, *54*, 58.
[10] J. F. M. Oudenhoven, L. Baggetto, P. H. L. Notten, *Adv. Energy Mater.* **2011**, *1*, 10.
[11] J. W. Long, B. Dunn, D. R. Rolison, H. S. White, *Chem. Rev.* **2004**, *104*, 4463.
[12] K. Sun, T.-S. Wei, B. Y. Ahn, J. Y. Seo, S. J. Dillon, J. A. Lewis, *Adv. Mater.* **2013**, *25*, 4539.
[13] S. Ferrari, M. Loveridge, S. D. Beattie, M. Jahn, R. J. Dashwood, R. Bhagat, *J. Power Sources* **2015**, *286*, 25.
[14] M. Nathan, D. Golodnitsky, V. Yufit, E. Strauss, T. Ripenbein, I. Shechtman, S. Menkin, E. Peled, *J. Microelectromech. Syst.* **2005**, *14*, 879.
[15] D. Golodnitsky, M. Nathan, V. Yufit, E. Strauss, K. Freedman, L. Burstein, A. Gladkich, E. Peled, *Solid State Ionics* **2006**, *177*, 2811.
[16] A. Patil, V. Patil, D. Wook Shin, J.-W. Choi, D.-S. Paik, S.-J. Yoon, *Mater. Res. Bull.* **2008**, *43*, 1913.
[17] P. H. L. Notten, F. Roozeboom, R. A. H. Niessen, L. Baggetto, *Adv. Mater.* **2007**, *19*, 4564.
[18] L. Baggetto, R. A. H. Niessen, F. Roozeboom, P. H. L. Notten, *Adv. Funct. Mater.* **2008**, *18*, 1057.

[19] H. Knoops, M. E. Donders, L. Baggetto, M. C. Van de Sanden, P. Notten, W. M. Kessels, *ECS Trans.* **2009**, *25*, 333.
[20] P. Schichtel, M. Geiß, T. Leichtweiß, J. Sann, D. A. Weber, J. Janek, *J. Power Sources* **2017**, *360*, 593.
[21] P. Knauth, *Solid State Ionics* **2009**, *180*, 911.
[22] J. Janek, W. G. Zeier, *Nat. Energy* **2016**, *1*, 16141.
[23] V. Thangadurai, S. Narayanan, D. Pinzaru, *Chem. Soc. Rev.* **2014**, *43*, 4714.
[24] R. Murugan, V. Thangadurai, W. Weppner, *Angew. Chem., Int. Ed.* **2007**, *46*, 7778.
[25] J. van den Broek, S. Afyon, J. L. M. Rupp, *Adv. Energy Mater.* **2016**, *6*, 1600736.
[26] J. van den Broek, J. L. M. Rupp, S. Afyon, *J. Electroceram.* **2017**, *38*, 182.
[27] M. Kotobuki, K. Kanamura, Y. Sato, T. Yoshida, *J. Power Sources* **2011**, *196*, 7750.
[28] S. Ohta, T. Kobayashi, T. Asaoka, *J. Power Sources* **2011**, *196*, 3342.
[29] C. Hansel, S. Afyon, J. L. M. Rupp, *Nanoscale* **2016**, *8*, 18412.
[30] L. Porz, T. Swamy, B. W. Sheldon, D. Rettenwander, T. Frömling, H. L. Thaman, S. Berendts, R. Uecker, W. C. Carter, Y.-M. Chiang, *Adv. Energy Mater.* **2017**, *7*, 1701003.
[31] K. Park, B.-C. Yu, J.-W. Jung, Y. Li, W. Zhou, H. Gao, S. Son, J. B. Goodenough, *Chem. Mater.* **2016**, *28*, 8051.
[32] Y. Li, B. Xu, H. Xu, H. Duan, X. Lü, S. Xin, W. Zhou, L. Xue, G. Fu, A. Manthiram, J. B. Goodenough, *Angew. Chem., Int. Ed.* **2017**, *56*, 753.
[33] R. Wagner, G. J. Redhammer, D. Rettenwander, A. Senyshyn, W. Schmidt, M. Wilkening, G. Amthauer, *Chem. Mater.* **2016**, *28*, 1861.
[34] H. Buschmann, J. Dolle, S. Berendts, A. Kuhn, P. Bottke, M. Wilkening, P. Heitjans, A. Senyshyn, H. Ehrenberg, A. Lotnyk, V. Duppel, L. Kienle, J. Janek, *Phys. Chem. Chem. Phys.* **2011**, *13*, 19378.
[35] E. Rangasamy, J. Wolfenstine, J. Sakamoto, *Solid State Ionics* **2012**, *206*, 28.
[36] H. El Shinawi, J. Janek, *J. Power Sources* **2013**, *225*, 13.
[37] S. Afyon, F. Krumeich, J. L. M. Rupp, *J. Mater. Chem. A* **2015**, *3*, 18636.
[38] C. Bernuy-Lopez, W. Manalastas, J. M. Lopez del Amo, A. Aguadero, F. Aguesse, J. A. Kilner, *Chem. Mater.* **2014**, *26*, 3610.
[39] T. Thompson, J. Wolfenstine, J. L. Allen, M. Johannes, A. Huq, I. N. David, J. Sakamoto, *J. Mater. Chem. A* **2014**, *2*, 13431.
[40] W. Gu, M. Ezbiri, R. Prasada Rao, M. Avdeev, S. Adams, *Solid State Ionics* **2015**, *274*, 100.
[41] S. Adams, R. P. Rao, *J. Mater. Chem.* **2012**, *22*, 1426.
[42] H. Buschmann, S. Berendts, B. Mogwitz, J. Janek, *J. Power Sources* **2012**, *206*, 236.
[43] J. L. Allen, J. Wolfenstine, E. Rangasamy, J. Sakamoto, *J. Power Sources* **2012**, *206*, 315.
[44] Y. Li, J.-T. Han, C.-A. Wang, H. Xie, J. B. Goodenough, *J. Mater. Chem.* **2012**, *22*, 15357.
[45] R.-J. Chen, M. Huang, W.-Z. Huang, Y. Shen, Y.-H. Lin, C.-W. Nan, *J. Mater. Chem. A* **2014**, *2*, 13277.
[46] K. Tadanaga, H. Egawa, A. Hayashi, M. Tatsumisago, J. Mosa, M. Aparicio, A. Duran, *J. Power Sources* **2015**, *273*, 844.
[47] M. Bitzer, T. Van Gestel, S. Uhlenbruck, Hans-Peter-Buchkremer, *Thin Solid Films* **2016**, *615*, 128.
[48] D. J. Kalita, S. H. Lee, K. S. Lee, D. H. Ko, Y. S. Yoon, *Solid State Ionics* **2012**, *229*, 14.
[49] J. Nong, H. Xu, Z. Yu, G. Zhu, A. Yu, *Mater. Lett.* **2015**, *154*, 167.
[50] S. Lobe, C. Dellen, M. Finsterbusch, H. G. Gehrke, D. Sebold, C. L. Tsai, S. Uhlenbruck, O. Guillon, *J. Power Sources* **2016**, *307*, 684.
[51] H. Katsui, T. Goto, *Thin Solid Films* **2015**, *584*, 130.
[52] C. Loho, R. Djenadic, M. Bruns, O. Clemens, H. Hahn, *J. Electrochem. Soc.* **2017**, *164*, A6131.
[53] S. Kim, M. Hirayama, S. Taminato, R. Kanno, *Dalt. Trans.* **2013**, *42*, 13112.
[54] J. Tan, A. Tiwari, *ECS Solid State Lett.* **2012**, *1*, Q57.
[55] J. S. Park, L. Cheng, V. Zorba, A. Mehta, J. Cabana, G. Chen, M. M. Doeff, T. J. Richardson, J. H. Park, J.-W. Son, W.-S. Hong, *Thin Solid Films* **2015**, *576*, 55.
[56] M. Rawlence, I. Garbayo, S. Buecheler, J. L. M. Rupp, *Nanoscale* **2016**, *8*, 14746.
[57] J. L. M. Rupp, E. Fabbri, D. Marrocchelli, J.-W. Han, D. Chen, E. Traversa, H. L. Tuller, B. Yildiz, *Adv. Funct. Mater.* **2014**, *24*, 1562.
[58] S. Schweiger, M. Kubicek, F. Messerschmitt, C. Murer, J. L. M. Rupp, *ACS Nano* **2014**, *8*, 5032.
[59] S. Schweiger, R. Pfenninger, W. J. Bowman, U. Aschauer, J. L. M. Rupp, *Adv. Mater.* **2017**, *29*, 1605049.
[60] Y. Shi, A. H. Bork, S. Schweiger, J. L. M. Rupp, *Nat. Mater.* **2015**, *14*, 721.
[61] J. Awaka, A. Takashima, H. Hayakawa, N. Kijima, Y. Idemoto, J. Akimoto, *Key Eng. Mater.* **2011**, *485*, 99.
[62] L. Kong, I. Karatchevtseva, D. J. Gregg, M. G. Blackford, R. Holmes, G. Triani, *J. Am. Ceram. Soc.* **2013**, *96*, 935.
[63] B. Paul, K. Singh, T. Jaroń, A. Roy, A. Chowdhury, *J. Alloys Compd.* **2016**, *686*, 130.
[64] K. Knoth, R. Hühne, S. Oswald, L. Schultz, B. Holzapfel, *Acta Mater.* **2007**, *55*, 517.
[65] F. Tietz, T. Wegener, M. T. Gerhards, M. Giarola, G. Mariotto, *Solid State Ionics* **2013**, *230*, 77.
[66] M. Stojmenović, S. Bošković, S. Zec, B. Babić, B. Matović, D. Bučevac, Z. Dohčević-Mitrović, F. Aldinger, *J. Alloys Compd.* **2010**, *507*, 279.
[67] J. L. M. Rupp, B. Scherrer, L. J. Gauckler, *Phys. Chem. Chem. Phys.* **2010**, *12*, 11114.
[68] G. Larraz, A. Orera, M. L. Sanjuan, *J. Mater. Chem. A* **2013**, *1*, 11419.
[69] S. Mukhopadhyay, T. Thompson, J. Sakamoto, A. Huq, J. Wolfenstine, J. L. Allen, N. Bernstein, D. A. Stewart, M. D. Johannes, *Chem. Mater.* **2015**, *27*, 3658.
[70] M. Kitajima, *Crit. Rev. Solid State Mater. Sci.* **1997**, *22*, 275.
[71] G. Gouadec, P. Colomban, *Prog. Cryst. Growth Charact. Mater.* **2007**, *53*, 1.
[72] J. W. Seo, J. Fompeyrine, A. Guiller, G. Norga, C. Marchiori, H. Siegwart, J.-P. Locquet, *Appl. Phys. Lett.* **2003**, *83*, 5211.
[73] Y. Tabira, R. L. Withers, T. Yamada, N. Ishizawa, *Z. Kristallogr.—Cryst. Mater.* **2001**, *216*, 92.
[74] T. Hagiwara, H. Yamamura, H. Nishino, *J. Soc. Inorg. Mater. Japan* **2010**, *17*, 359.
[75] Y. Tabira, R. L. Withers, L. Minervini, R. W. Grimes, *J. Solid State Chem.* **2000**, *153*, 16.
[76] Y. Chen, E. Rangasamy, C. Liang, K. An, *Chem. Mater.* **2015**, *27*, 5491.
[77] R. Eason, *Pulsed Laser Deposition of Thin Films: Applications-Led Growth of Functional Materials*, Wiley, Hoboken **2007**.
[78] Q. A. Islam, S. Nag, R. N. Basu, *Mater. Res. Bull.* **2013**, *48*, 3103.
[79] G. Ou, W. Liu, L. Yao, H. Wu, W. Pan, *J. Mater. Chem. A* **2014**, *2*, 1855.
[80] K. L. Ngai, E. Riande, G. B. Wright, A. Bunde, M. D. Ingram, P. Maass, *J. Non-Cryst. Solids* **1994**, *172*, 1222.
[81] A. I. Frenkel, D. Ehre, V. Lyahovitskaya, L. Kanner, E. Wachtel, I. Lubomirsky, *Phys. Rev. Lett.* **2007**, *99*, 215502.
[82] D. Ehre, H. Cohen, V. Lyahovitskaya, I. Lubomirsky, *Phys. Rev. B* **2008**, *77*, 184106.
[83] M. Ohring, *Materials Science of Thin Films*, Academic Press, San Diego **2002**.
[84] R. Mercier, J. Malugani, B. Fahys, G. Robert, *Solid State Ionics* **1981**, *5*, 663.
[85] M. H. Braga, N. S. Grundish, A. J. Murchison, J. B. Goodenough, J. B. Goodenough, *Energy Environ. Sci.* **2017**, *10*, 331.